JOURNAL OF SPACECRAFT AND ROCKETS
Vol. 45, No. 2, March–April 2008

In Situ Navigation of Spacecraft Formations in High-Altitude and Extraterrestrial Orbits

Greg N. Holt* and E. G. Lightsey†
The University of Texas at Austin, Austin, Texas 78712

DOI: 10.2514/1.29361

An investigation was performed to evaluate sensor suitability and performance for formation flying in a variety of spaceborne environments. This was done as a precursor to the development of strategies for novel uses of satellite formations in environments other than low Earth orbit. Sensor models were developed to allow for a uniform treatment in processing range measurements. A formation simulation environment was then produced that included representative formation geometries, sensor noises, and navigation filters. The formations studied included highly elliptical and libration point orbits. The equations of motion were modified to account for a more accurate propagation of elliptical orbits, and an estimator was designed that allowed for large propagation times without global positioning system measurements. A high-accuracy transponder measurement was added and evaluated to give improved performance to accuracies of a few meters. A similar study was performed for the libration point orbit without the capability to track global positioning system signals.

Nomenclature

a_0	=	frequency drift, s/s^2
c	=	speed of light, m/s
d_0	=	clock drift, s/s
m	=	spacecraft mass, kg
$\frac{m}{C_D A}$	=	satellite ballistic coefficient, kg/m^2
$R_{\mathrm{SAT}i}$	=	range to formation member i, m
$R\|_{t_e}$	=	true scalar range at signal receipt (end), m
$R_\oplus$	=	Earth radius, m
r	=	radius of satellite orbit, m
$r_{i,j,k}$	=	satellite position vector components in Earth centered frame, m
$\boldsymbol{r}_{\mathrm{LOS}}$	=	line-of-sight vector to other formation member, m
$\boldsymbol{r}_{\mathrm{sat}-M}$	=	vector from satellite to moon, m
$\boldsymbol{r}_{\oplus-M}$	=	vector from Earth to moon, m
$\boldsymbol{r}_{\oplus-\mathrm{sat}}$	=	vector from Earth to satellite, m
t_0	=	reference epoch for clock parameters, s
$\boldsymbol{v}$	=	relative velocity between satellite and atmosphere, m/s
μ	=	mass ratio of the restricted three-body problem
μ_M	=	moon gravitational parameter, m^3/s^2
$\mu_\oplus$	=	Earth gravitational parameter, m^3/s^2
ν	=	unmodelled error contributions, m
ρ_{atm}	=	atmospheric density, kg/m^3
$\phi(t_0)$	=	clock bias, s

Introduction

THIS study presents a generalized approach to modelling range measurements in a relative positioning algorithm. The advantages to this approach are twofold. First, scenario simulations can easily be adapted to incorporate single or multiple sensors for relative navigation. Second, results from these scenarios can be compared because the underlying range measurement equations use common error models. A new formulation of the two-way radio-navigation problem is presented as an example.

An important contribution of this research is the generalization of high-fidelity ranging equations for formation flying sensors. These formulations are used in the sensor models and demonstrated in simulation with representative estimation techniques for various formation flying scenarios. These quantifiable error models allow mission designers to adopt a uniform approach to comparing and selecting formation sensors for different missions.

For formations in highly elliptical Earth orbits (HEO), where absolute references such as the global positioning system (GPS) may have outages, a sample relative navigation (relnav) estimator is designed that accounts for these outages and expected disturbances. In addition, the equations of motion in this estimator are tailored for more accurate HEO propagation. Similarly, a sample relnav filter is presented for a formation in a libration orbit where external measurements are very rare. All of these scenarios can be compared because the underlying measurements used by the filters come from the aforementioned generalized ranging models.

A demonstration is given appending new measurement types to an existing filter to perform sensor fusion. The example shown is for two-way ranging, but could be extended to other sensor types perhaps not yet defined or invented.

Sensor Model

The time-of-flight sensor methodology involves measuring the time taken by a transmitted signal while travelling a defined path. Multiplying the signal propagation time by the speed of light gives the path length and range. This may be accomplished by using one-way or two-way signals. Figures 1a and 1b show the signal paths that are used in one-way and two-way ranging, respectively. One-way time-of-flight ranging is perhaps best known as the fundamental measurement of the U.S. global positioning system (GPS) [1]. It can, however, be used in other radio-navigation schemes as well. A transmitter sends a signal at start time t_s and it is received at end time t_e. During that interval, the transmitter has moved to a final relative position $\boldsymbol{R}|_{te}$. The projection of that change along the line of sight is denoted by $\Delta\rho$. If multiple transmitters at known locations are used, the receiver can determine its position.

In two-way time-of-flight ranging, the fundamental measurement is accomplished by noting the time it takes for a transmitted signal to reach a transponder, undergo retransmission, and travel back to the original sender. The transceiver sends a signal at start time t_s, it is received and rebroadcast by a transponder at time t_t, and is finally

Presented as Paper 6755 at the AIAA Guidance, Navigation and Control Conference and Exhibit, Hilton Head, SC, 20–23 August 2007; received 18 December 2006; revision received 23 October 2007; accepted for publication 23 October 2007.

*Ph.D. Graduate, Department of Aerospace Engineering and Engineering Mechanics. Member AIAA.

†Associate Professor, Department of Aerospace Engineering and Engineering Mechanics. Associate Fellow AIAA.

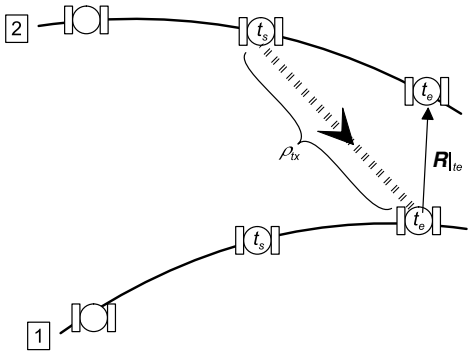

a) One-way RF

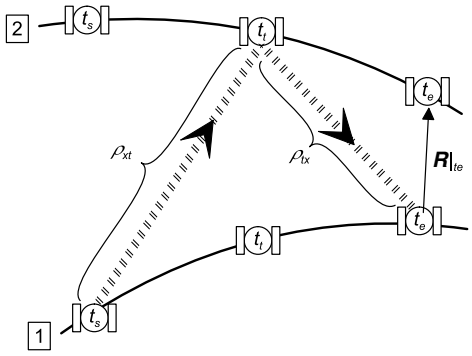

b) Two-way RF

Fig. 1 Vector measurement diagrams.

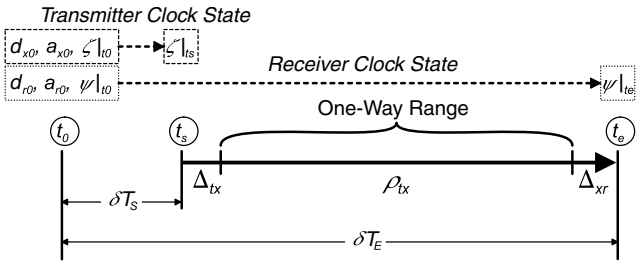

a) One way

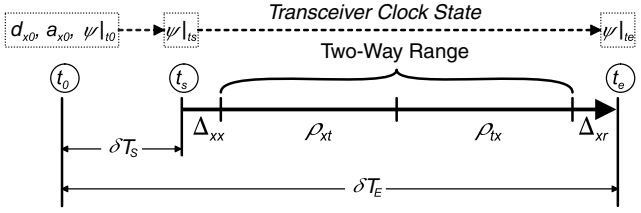

b) Two way

Fig. 2 Time-of-flight measurements.

received by the transceiver at end time t_e. During the entire interval, the transceiver has changed position, and the projection of that change along the line of sight is $\Delta\rho_1$. During the return trip interval, the transponder has moved by a projected amount $\Delta\rho_2$. Once multiple transponder measurements are taken, the sender can determine its position.

Mathematical Representation

Measuring the time of flight of a radio signal generally involves a phase measurement from either a generated code or the carrier wave itself. Both the transmitter and receiver will perform their operations using internal clocks, and any discrepancy between these clocks and an overall "system time" will cause a measurement bias. Typically, this bias is estimated along with the vehicle state in the navigation filter. The measurement itself, commonly referred to as the pseudorange, is the combination of the geometric range, the overall clock bias, and any other modeled or unmodelled error sources. Figures 2a and 2b graphically show the development of the time-of-flight measurements. It is notable that the one-way measurement contains contributions from both the transmitter and receiver clocks, whereas the two-way measurement only has components from the transceiver clock. The one-way time-of-flight measurement is shown in Eq. (2). This formulation is well defined in GPS literature such as Misra and Enge [2] and Kaplan [1].

One-way geometric range:

$$R|_{te} = c(t_e - t_s) + \Delta\rho \tag{1}$$

One-way pseudorange:

$$\begin{aligned}\rho &= c[(t_e + \psi|_{te}) - (t_s + \zeta|_{ts})] + \Delta\rho + c\Delta_{tx} + c\Delta_{xr} + \nu \\ &= c(t_e - t_s) + c(\psi|_{te} - \zeta|_{ts}) + c\Delta_{tx} + c\Delta_{xr} + \nu \\ &= R|_{te} + c\delta t + c(\Delta_{tx} + \Delta_{xr}) + \nu\end{aligned} \tag{2}$$

where t_s is the system time at which the signal left the transmitter, t_e is the system time at which the signal reached the transmitter, $\zeta|_{ts} = \zeta(t_s)$ is the transmitter clock state at t_s, $\psi|_{te} = \psi(t_e)$ is the receiver clock bias state at t_e, $\delta t = \zeta|_{ts} + \psi|_{te}$ is the overall clock bias contribution, $\Delta\rho$ is the transmitter position change projection along the line-of-sight direction, Δ_{tx} is the transmitter line delay, and Δ_{xr} is the receiver line delay.

The two-way time-of-flight measurement is shown mathematically in Eq. (4). This has been used previously in ground tracking systems such as NASA's Deep Space Network (DSN) [3,4]. The two-way time-of-flight measurement is presented here in a parallel formulation to the one-way time-of-flight measurement as a demonstration of how ranging measurements from new sensors can be expressed in a comparable form. This formulation also facilitates incorporation of the additional sensor into existing navigation routines.

Two-way geometric range:

$$2R|_{te} = c(t_e - t_s) + (\Delta\rho_1 + \Delta\rho_2) = c(t_e - t_s) + \Delta\rho \tag{3}$$

Two-way pseudorange:

$$\begin{aligned}\rho &= c[(t_e + \psi|_{te}) - (t_s + \psi|_{ts})] + \Delta\rho + c\Delta_{xx} \\ &\quad + c\Delta_{xr} + c(\psi|_{te} - \psi|_{ts}) + \nu \\ &= c(t_e - t_s) + \Delta\rho + c\delta t + c(\Delta_{xx} + \Delta_{xr}) + \nu \\ &= 2R|_{te} + c(\psi|_{te} - \psi|_{ts}) + c(\Delta_{xx} + \Delta_{xr}) + \nu\end{aligned} \tag{4}$$

where t_s is the system time at which the original signal left the transceiver, t_e is the system time at which the return signal reached the transceiver, $\psi|_{ts} = \psi(t_s)$ is the clock state at t_s, $\psi|_{te} = \psi(t_e)$ is the clock state at t_e, $\delta t = \psi|_{ts} + \psi|_{te}$ is the overall clock bias, $\Delta\rho_1$ is the change in position of the transceiver during the signal round trip projected along the line-of-sight direction, $\Delta\rho_2$ is the change in position of the transponder during the signal return trip projected along the line-of-sight direction, Δ_{xx} is the transceiver transmit line delay, and Δ_{xr} is the transceiver receive line delay.

Sensor Architecture

The sensor hardware for one-way and two-way ranging share many attributes. Sample architectures are shown in Figs. 3a and 3b. As these figures show, the two-way method can be thought of as an extended case of the one-way method with each member having both transmit and receive capabilities. Both the signal generation and measurement processes use a local frequency standard, typically in the form of a thermally or numerically controlled oscillator. For increased ranging and navigation accuracy, one or both may have an ultrastable oscillator. All radio-navigation systems have line biases associated with the transmission and receiver hardware as well.

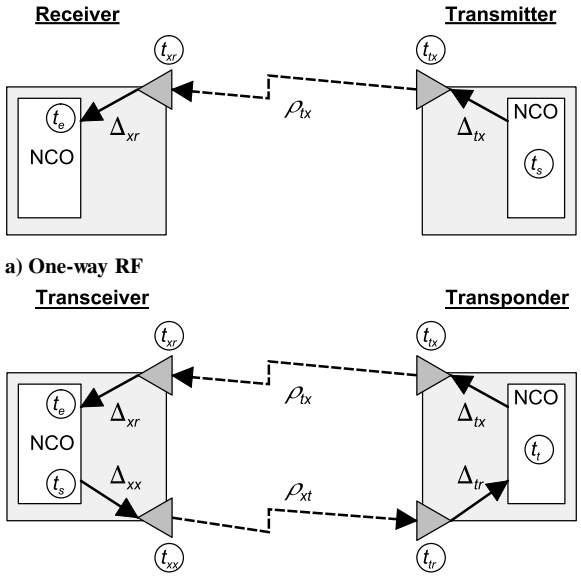

Fig. 3 Measurement-type diagrams.

A key consideration for the two-way measurement type is the time delay in the retransmission of the signal at the transponder. As Fig. 3b shows, there are line biases and internal effects that can contribute errors to the pseudorange. A solution to this dilemma is proposed by Ely [5], in which a phase-coherent turnaround scheme is used to remove these biases and have the transponder function as a true signal reflector.

Clock Considerations

Any timed radio-navigation solution will depend upon a reference oscillator, or clock, to generate signals for transmission and/or phase comparison. Any unmodelled errors in the clock will propagate through the solution process as errors in navigation. Clock error modelling and removal, then, becomes an important part of the radio-navigation solution. The clock bias is modeled as a random walk process associated with the integral of the white noise oscillator frequency [5]. To estimate the clock state in a navigation filter, this is typically represented by a Taylor series expansion as in Eq. (5).

$$\phi(t) = \phi(t_0) + d_0(t - t_0) + a_0(t - t_0)^2 + \cdots \tag{5}$$

The state vector for the satellite can include any number of these clock terms, but typically just the first two are considered. As will be shown later in the simulations, these two terms will give a good representation of the clock for the filter models used in the following sections.

When constructing a navigation simulation, realistic clock performance is important because it is typically the dominant error source in the pseudorange measurement. A detailed explanation of clock models can be found in Parkinson and Spilker [6], in which the standard metric of *power spectral density* is defined for frequency stability. In simulations for this study, standard oscillators are modeled with white noise power spectral densities of 4×10^{-19} m^2/s and 1.58×10^{-18} m^2/s^3, whereas ultrastable oscillators are modeled with 2×10^{-26} m^2/s and 7.89×10^{-25} m^2/s^3 [7].

Highly Elliptical Orbit Formations

A satellite formation in HEO is of great interest to many mission designers. Carpenter et al. [8] describe an HEO formation, the Magnetospheric Multiscale (MMS) mission, as a benchmark problem. The navigation task, however, becomes increasingly difficult as the distance from Earth increases. Specifically, the signals from the terrestrial global positioning system satellites become harder to track and in many cases are altogether unavailable. It may be necessary, therefore, to augment the formation navigation capability using additional sensors to achieve needed navigation performance. Radio frequency (RF) transceiver measurements between formation members have been proposed as one method of supplying this additional information.

Table 1 Simulated HEO orbit mean elements

Element	Value	Units
a	61277	km
e	0.875	none
i	0	deg
Ω	0	deg
ω	90	deg

The formation that was simulated for this study was based upon the benchmark orbit suggested by Carpenter et al.[8]. This case study was performed as an example of the many potential applications of the method. It is not intended to reproduce or to validate previously published results for MMS, although the results are similar [9,10]. Although the details vary from case to case, the estimation process is general. For this study, the sensor models developed in the previous sections were implemented into a dynamic simulation of an elliptical orbit. For a trajectory simulation, the reference orbit is summarized in Table 1 and is shown in Fig. 4.

The reference trajectory is propagated under the influence of Earth's gravity and some of the major perturbing forces of the terrestrial orbital environment. The perturbations include the following:

1) *Nonspherical Gravity*: The effect of asymmetric Earth gravity is modeled by inclusion of the effect of the first spherical harmonic term, commonly known as J_2 [11].

$$\begin{aligned} a_i &= \frac{-3J_2\mu_\oplus R_\oplus^2 r_i}{2r^5}\left(1 - \frac{5r_k^2}{r^2}\right) \\ a_j &= \frac{-3J_2\mu_\oplus R_\oplus^2 r_j}{2r^5}\left(1 - \frac{5r_k^2}{r^2}\right) \\ a_k &= \frac{-3J_2\mu_\oplus R_\oplus^2 r_k}{2r^5}\left(3 - \frac{5r_k^2}{r^2}\right) \end{aligned} \tag{6}$$

where

$$\boldsymbol{a} = a_i\hat{i} + a_j\hat{j} + a_k\hat{k} = \text{ acceleration } (\text{m/s}^2) \tag{7}$$

2) *Lunar Third-Body Effects*: The gravitational interaction of the moon with both the satellite and the Earth was modeled [11].

$$\boldsymbol{a} = -\frac{\mu_\oplus \boldsymbol{r}_{\oplus-\text{sat}}}{r_{\oplus-\text{sat}}^3} + \mu_M\left(\frac{\boldsymbol{r}_{\text{sat}-M}}{r_{\text{sat}-M}^3} - \frac{\boldsymbol{r}_{\oplus-M}}{r_{\oplus-M}^3}\right) \tag{8}$$

3) *Atmospheric Drag*: As the formation nears Earth at perigee, it is subject to drag in the upper levels of the atmosphere. This drag was modeled with assumed values for the mass and drag coefficient [11]. The relative velocity between the satellite and atmosphere was calculated with an assumed stationary atmosphere.

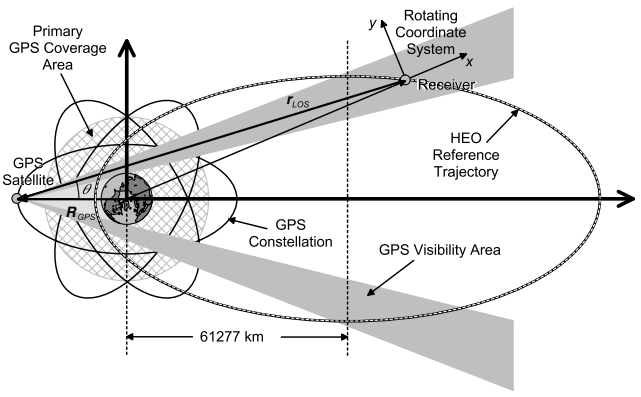

Fig. 4 HEO reference trajectory [8] with GPS observability.

$$\boldsymbol{a} = -\frac{1}{2}\rho_{\text{atm}}\frac{C_D A}{m}\left|v\right|\boldsymbol{v} \tag{9}$$

4) *Other Effects*: Two other disturbance effects that might be considered, depending on the application, are *solar radiation pressure* and *actuation perturbations*. A simple model for solar radiation pressure acceleration is [12]

$$|\boldsymbol{a}| = KAP/m \tag{10}$$

where K is a dimensionless constant between 0 and 2; A is the cross-sectional area of the spacecraft relative to the sun line, which is vehicle and attitude dependent;, and P is the momentum flux from the sun, which is approximately 4.4×10^{-6} kg $\cdot$ m^{-1} $\cdot$ s^{-2} for the Earth environment. The solar radiation pressure acceleration $\boldsymbol{a}$ is directed radially outward from the sun. Actuation perturbations are dependent on the vehicle and the method of actuation, for example, unbalanced gas jet propellant leakages. They may be significant for precision formation flying.

Although these effects may be needed for mission-specific high-fidelity navigation, they were intentionally left out of this study because the results are highly application dependent. Other types of perturbations are possible as well and would also be included here.

The simulated formation is built around the reference trajectory previously described and shown in Fig. 4. However, there is no spacecraft on the reference trajectory. The four spacecraft that make up the formation must form a 10 km regular tetrahedron at apogee. Close approaches of 1 km or less are prohibited in the specification.

This orbit is accomplished using the initial offsets from the nominal reference trajectory shown in Table 2.

The formation relative motion is shown in Fig. 5a. The motion shown in this figure is relative to the HEO reference trajectory in Fig. 4. At apogee, the formation assumes the regular tetrahedron specified in the requirements. Near perigee, however, the formation tends to "flatten" and becomes planar in two places. The formation separation distances are shown in Fig. 5b. There are no approaches within the specified 1 km exclusion area.

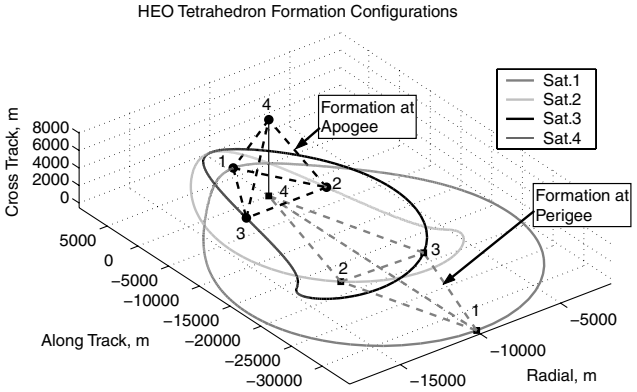

a) Formation setup in HEO

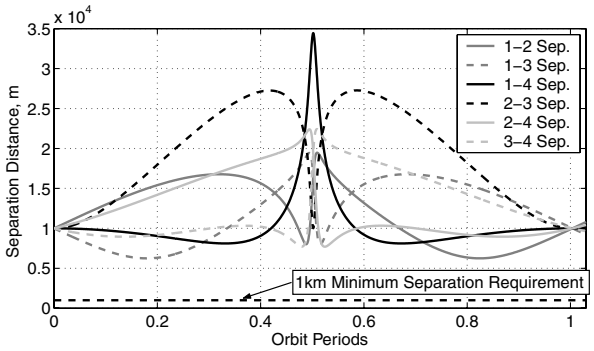

b) Separation distances

Fig. 5 Tetrahedron formation characteristics.

Estimation Technique

For simulations in this study, an eight-element relative state vector was used consisting of position, velocity, and local oscillator terms. The position and velocity components are all given relative to the reference orbit.

$$\boldsymbol{X} = \begin{bmatrix} x_{\text{rel}}\ (\text{m}) \\ y_{\text{rel}} \\ z_{\text{rel}} \\ \dot{x}_{\text{rel}}\ (\text{m/s}) \\ \dot{y}_{\text{rel}}\ (\text{m/s}) \\ \dot{z}_{\text{rel}}\ (\text{m/s}) \\ c\delta t\ (\text{m}) \\ c\dot{\delta} t\ (\text{m/s}) \end{bmatrix} \tag{11}$$

Estimating the relative states of satellites in the formation is accomplished by the use of a Kalman filter, a common name for the sequential filter. The Kalman filter is able to accumulate measurements over extended time intervals to improve its estimation accuracy. The type and weighting of the measurements in the Kalman filter will depend upon the particular orbit and sensors involved. The general form of the Kalman filter used in this study follows the setup described by Tapley et al. [13].

Table 2 Initial formation offsets

Offset	Sat 1	Sat 2	Sat 3	Sat 4
x_{rel}, m	0	5000	-5000	0
y_{rel}, m	$10,000/\sqrt{3}$	$-5000/\sqrt{3}$	$-5000/\sqrt{3}$	0
z_{rel}, m	0	0	0	$10,000\sqrt{2/3}$
$\dot{x}_{\text{rel}}$, m/s	0	0.05	0.05	0
$\dot{y}_{\text{rel}}$, m/s	0	-0.258	0.258	0
$\dot{z}_{\text{rel}}$, m/s	0	0	0	0

The Kalman filter dynamic model was derived from the relative equations of motion for bodies in elliptical orbits set out by Broucke [14]. These equations require knowledge of the reference orbit eccentricity (e), semimajor axis (a), and true anomaly (ν). The motion is assumed to be two-body, point mass dynamics with no perturbations based on the reference frame shown in Fig. 4.

$$\ddot{x}_{\text{rel}} - 2\dot{\theta}\dot{y}_{\text{rel}} - \dot{\theta}^2 x_{\text{rel}} - \ddot{\theta} y_{\text{rel}} = 2x_{\text{rel}}\left(\frac{\mu}{r_1^3}\right)$$

$$\ddot{y}_{\text{rel}} + 2\dot{\theta}\dot{x}_{\text{rel}} - \dot{\theta}^2 y_{\text{rel}} + \ddot{\theta}x + rel = -y_{\text{rel}}\left(\frac{\mu}{r_1^3}\right) \qquad \ddot{z}_{\text{rel}} = -\left(\frac{\mu}{r_1^3}\right) \tag{12}$$

where

$$r_1 = \frac{a(1-e^2)}{(1+e\cos\nu)} \tag{13}$$

$$\dot{\theta} = \sqrt{\mu(a(1-e^2))}/r_1^2 \tag{14}$$

$$\ddot{\theta} = -2\mu e \sin\nu / r_1^3 \tag{15}$$

Because these equations are linear with respect to the relative states, a Kalman filter is sufficient for the estimation of the relative states. The Eqs. (6–9) represent dynamic mismodelling in the estimation because they are not included in the dynamic model given by Eqs. (12–15).

Effects of Attitude/Range Coupling: It is important to note that these equations only track the satellite's center of mass. In actuality, there will be a moment arm between the center of mass and the sensor (usually an antenna) that will result in attitude/range measurement coupling. For a given line of sight to the signal transmitter $\boldsymbol{s}$ and

moment arm $\boldsymbol{b}$, the attitude/range measurement contribution Δr is

$$\Delta r = \boldsymbol{s} \cdot \boldsymbol{b} = (\boldsymbol{s})_E^T \boldsymbol{b}_E = (\boldsymbol{s})_E^T A_{B>E} \boldsymbol{b}_B \tag{16}$$

where the subscript E denotes the external reference frame and the subscript B indicates the body-fixed reference frame. $A_{B>E}$ is the 3×3 direction cosine matrix that transforms a vector from the B frame to the E frame.

If the attitude of the vehicle is not included in the range measurement model, it will result in an unmodeled error up to the dimension of the moment arm, which will typically be 1–2 m for most spacecraft. An error of this scale will definitely affect the resulting navigation measurement accuracy unless it is properly modeled.

Nevertheless, this study does not model the attitude motions of the vehicle in its simulations. Any such simulation would be hypothetical and application specific. Instead, it is assumed that attitude corrections will be measured and removed in the manner of Eq. (16) in tandem with processing the range measurements for an actual spacecraft application.

GPS-Only Estimation

One possibility for the relative navigation of the formation is the use of GPS receivers and a simple data-exchange crosslink with no intersatellite measurements. This allows absolute positioning and relative navigation.

GPS Visibility

To calculate the visibility of individual GPS satellites in the simulation, two regimes were considered.

1) *Low Altitude* ($<\frac{3}{4}$ GPS radius): For satellites with orbital position $r < \frac{3}{4} R_{\text{GPS}} \approx 20,000$ km, direct tracking of the overhead signal of visible GPS satellites is possible. This distance is not a rigorous indicator for the range of allowable GPS signal reception. This study does not take into account the narrow Earth-directed GPS transmission beams, which may result in signal dropouts before this distance is reached. GPS signals will be difficult to acquire at higher altitudes due to link properties [15]. The effect could result in a "dead zone" region where GPS measurements are extremely sparse. This algorithm would provide only time updates in this region for the GPS-only case. If it was important to receive measurement updates in this region, another measurement sensor such as a ground-based system or the relative navigation transponder system proposed in this paper might be used to augment the GPS-only design.

Given an elevation mask α, compute the angle to an individual GPS satellite by

$$\theta = \cos^{-1}(\hat{R} \cdot \boldsymbol{r}_{\text{LOS}}) \tag{17}$$

where $\hat{R}$ is the unit vector from Earth to the receiver and $\boldsymbol{r}_{\text{LOS}}$ is the line-of-sight vector from the receiver to the GPS satellite under consideration. The GPS satellite is then visible in this low altitude region when

$$\theta_{\text{visible}} < 90 \text{ deg} - \alpha \tag{18}$$

2) *High Altitude* ($>\frac{3}{4}$ GPS radius): For satellites with radius distances approaching and above the GPS constellation altitude $r > \frac{3}{4} R_{\text{GPS}} \approx 20,000$ km, it is possible that GPS satellites transmitting through the Earth limb will be visible to high-gain directional antennas on the receiving spacecraft. This region is shown, for example, as the gray banded region in Fig. 4. Although there are dynamic range and link budget challenges with tracking the GPS signal, it is possible that a suitably equipped receiver with spacecraft attitude control could track and collect some of these signals. Falcon Gold is an example of a historical mission that has collected GPS measurements at and above the GPS constellation altitude [15].

Assuming that the GPS satellites are nominally Earth pointed and modeled with a main broadcast cone of $\approx$42.5 deg, the visibility at high altitudes can be calculated by removing that portion of the RF cone that is blocked by the Earth (Fig. 4). At GPS radius, this amounts to 27.8 deg of obscuration [16].

$$\theta = \cos^{-1}(-\hat{R}_{\text{GPS}} \cdot \boldsymbol{r}_{\text{LOS}}) \tag{19}$$

where $\hat{R}_{\text{GPS}}$ is the unit vector from Earth to the GPS satellite and $\boldsymbol{r}_{\text{LOS}}$ is the line-of-sight vector from the receiver to the GPS satellite under consideration. The GPS satellite is then visible when

$$27.8 \text{ deg} < \theta_{\text{visible}} < 42.5 \text{ deg} \tag{20}$$

It is assumed that the appropriate measures have been taken with the antenna and receiver design so that when a GPS signal is visible, it may be tracked. This presumes some advances in GPS receiver design, because most current GPS receivers are not capable of operating in this regime.

Filter Regimes

Different filter regimes were established based on the orbit altitude and number of GPS satellites tracked. All use the identical information matrices

$$H_{\text{GPS}_i^x} = [\boldsymbol{r}_{\text{LOS}_i^x} \;\; 0 \;\; 0 \;\; 0 \;\; 1 \;\; 0] \tag{21}$$

$$H_{\text{RGPS}_{i,j}^x} = H_{\text{GPS}_i^x} - H_{\text{GPS}_j^x} \tag{22}$$

$$= [(\boldsymbol{r}_{\text{LOS}_i^x} - \boldsymbol{r}_{\text{LOS}_j^x}) \;\; 0 \;\; 0 \;\; 0 \;\; 0 \;\; 0] \tag{23}$$

where $\boldsymbol{r}_{\text{LOS}_j^x}$ is the line-of-sight vector from formation member i to GPS satellite x.

1) *GPS Near*: When the formation is within three quarters of the GPS radius and two or more GPS satellites are tracked, the GPS-near regime is used. Here, relative navigation (RGPS) can be performed using carrier phase measurements on the formation to augment the code-based pseudorange measurements.

$$\tilde{H}_{\text{GPS-near}} = [H_{\text{GPS}_1} \;\; H_{\text{RGPS}_{1,2}} \;\; H_{\text{RGPS}_{1,3}} \;\; H_{\text{RGPS}_{1,4}}] \tag{24}$$

$$R_{\text{GPS-near}} = \begin{bmatrix} (10 \text{ m}) & & \cdots & 0 \\ & (1 \text{ m}) & & \vdots \\ \vdots & & (1 \text{ m}) & \\ 0 & \cdots & & (1 \text{ m}) \end{bmatrix} \tag{25}$$

$$y_{\text{GPS}^x} = R_{\text{GPS}^x} - (\rho_{\text{GPS}^x} + c\delta t) \tag{26}$$

$$y_{\text{RGPS}_{1,j}^{x,y}} = R_{\text{GPS}_1^x} - R_{\text{GPS}_1^y} - R_{\text{GPS}_j^x} + R_{\text{GPS}_j^y} - \rho_{\text{RGPS}_{1,j}^{x,y}} \tag{27}$$

$$y = [y_{\text{GPS}^1} \;\; \cdots \;\; y_{\text{RGPS}_{1,2}^{1,2}} \;\; y_{\text{RGPS}_{1,2}^{1,3}} \;\; \cdots] \tag{28}$$

The values chosen for the absolute and relative range measurement accuracy (10 and 1 m, respectively) are conservatively based on those that are readily achievable with current low-cost spaceborne GPS receivers [6]. The modeled GPS errors are based on the L1 code and carrier budgets given in Kaplan [1]. However, the example is intended mainly to demonstrate the modelling technique and application, and so the values chosen are not intended to be specialized to GPS sensors.

2) *GPS Far*: When the formation is outside of the area of primary GPS availability, there is still signal availability through the RF spillover from the GPS satellites on the far side of the Earth (Fig. 4). The number of visible satellites will be limited, whereas the long signal path and lack of geometric distribution make RGPS ineffective.

$$\tilde{H}_{\text{GPS-far}} = [H_{\text{GPS}}] \tag{29}$$

$$R_{\text{GPS-far}} = 10 \text{ m} \tag{30}$$

$$y_{\text{GPS}^x} = R_{\text{GPS}^x} - (\rho_{\text{GPS}^x} + c\delta t) \tag{31}$$

$$y = [y_{\text{GPS}^1} \quad y_{\text{GPS}^2} \quad \cdots] \tag{32}$$

In this analysis, the measurement error in the signal due to the longer path length is not considered. It is expected that the Earth limb measurements will be subjected to higher ionospheric delays and tracking loop errors. Because the magnitudes of these errors are not well known at this time, only a "typical" rms range measurement error of 10 m was used in the analysis. This number could be updated with more accurate information when it becomes available. In the event that it is critical to maximize the absolute navigation accuracy, a dual frequency receiver could be used to remove the ionospheric delay from the measurements.

3) *Dead Reckoning*: When no GPS measurements are available, the measurement accumulation and update portion of the Kalman filter algorithm are skipped and the estimated state positions and covariance are propagated ahead to the next epoch. Because the knowledge of the system dynamics does not include the unmodelled perturbations described earlier in Eqs. (6–9), large errors in the navigation state can be introduced by the time propagation step.

Transponder-Only Estimation

Another possibility for the relative navigation of the formation is the use of a high-accuracy transponder measurement between the formation members. This allows some precise navigation but, when used as the sole source of information, removes the capability to align with an external time source.

$$\tilde{H}_{\text{Transp}} = [(2\boldsymbol{r}_{\text{LOS}} + 4\delta t \boldsymbol{r}_{\text{LOS}}) \;\; 0 \;\; 0 \;\; 0 \;\; 0 \;\; 0 \;\; 0 \;\; 2\rho/c] \tag{33}$$

$$R_{\text{Transp}} = 10 \text{ m} \tag{34}$$

$$y_{\text{Transp}} = (2R_{\text{SAT}i} - 2\delta \dot{i} R_{\text{SAT}i}) - \rho_{\text{Transp}} \tag{35}$$

Transponder and GPS Estimation

Another possibility for the relative navigation of the formation is the use of the high-accuracy, intersatellite transponder in conjunction with the GPS receivers and a simple data-exchange crosslink.

$$\tilde{H}_{\text{Combo}} = [H_{\text{Transp}} \quad H_{\text{GPS}} \quad H_{\text{RGPS}} \quad H_{\text{RGPS}} \quad H_{\text{RGPS}}] \tag{36}$$

$$R_{\text{Combo}} = \begin{bmatrix} (10 \text{ m}) & \cdots & & & 0 \\ \vdots & (10 \text{ m}) & & & \\ & & (1 \text{ m}) & & \\ & & & (1 \text{ m}) & \vdots \\ 0 & & & \cdots & (1 \text{ m}) \end{bmatrix} \tag{37}$$

$$y_{\text{Combo}} = [y_{\text{Transp}} \quad y_{\text{GPS}} \quad y_{\text{RGPS}_{1,2}} \quad y_{\text{RGPS}_{1,3}} \quad y_{\text{RPGS}_{1,4}}] \tag{38}$$

The new measurement types are incorporated by "stacking" the measurement and noise matrices with the additional data type. By example, this demonstrates how to append new measurement types to an existing filter to perform the sensor fusion.

Simulation/Estimation Assumptions

Several assumptions were made in the design of the estimator and the simulation that are worth noting before examining the results. In all cases in which the carrier phase-range measurements were used, sensor accuracies were reported for these cases assuming that the integer cycle ambiguities had been properly resolved. This step is necessary to convert the carrier phase measurement to a valid range measurement. There are a wide range of techniques for resolving phase integers, and each have varying efficacy in different environments [1,2,6]. In addition, no simulation allowance is made for multipath at the receiving antenna. This will vary greatly depending upon the size and geometry of the chassis itself, and so these errors are left to the individual mission designer to consider. More information on these techniques is presented in Kaplan [1] and Hofmann-Wellenhoff [17].

The two cited topics, multipath and cycle ambiguity resolution, are related in terms of carrier phase measurement robustness. Cycle ambiguity resolution is subject to robustness considerations and these factors are amplified in the presence of large vehicle-induced multipath. Every reasonable effort should be made to mitigate multipath by locating the placement of the antennas in a way that will minimize reflections into the antenna element. Antenna choke rings have been used with success on some spacecraft missions.

This analysis does not directly address vehicle-induced multipath or cycle ambiguity resolution, which could be significant dissertations by themselves. Instead, the analysis is presented assuming these topics have been successfully managed. The nature of the filter design that is proposed partially mitigates the sensitivity of the navigation solution to short-term spikes and data dropouts due to these effects. Nonetheless, these topics should be carefully addressed in any actual design.

Another important consideration that is not detailed here is time synchronization. Accurate relative navigation depends upon the ability to compare timed measurements within the formation and with external references. Dynamic models often depend on accurate time synchronization as well. Time biases are presented here as estimated state errors but are not shown for their contribution to the navigation error.

HEO Results

All results presented are from the perspective of a single spacecraft (number 1 in Fig. 5a), as if the navigation filters are executing onboard that particular spacecraft. A true relative trajectory about the reference orbit is computed as part of the simulation, and the error results presented are deviations from that computed true trajectory. The clock error is modeled using the parameters specified in the section labeled "Clock Considerations". It is assumed that each member of the formation will be performing this task and exchanging estimated state information in the process.

GPS-Only Navigation

As discussed in the "GPS-Only Estimation" section, the first case uses only an onboard GPS and a simple data-exchange crosslink to perform differential GPS when visibility allows. Figure 6a shows the relative navigation errors over four orbit periods, beginning at apogee. There are noticeably large outlying measurements, up to and exceeding 2 km, especially during periods with little or no signal availability. Here the navigation filter can only perform dead reckoning in the presence of unmodelled perturbations. Near perigee, the formation enters a measurement-rich environment and the filter converges rapidly. A closer view is shown in Fig. 6b, in which the brief region of full-GPS coverage is seen to give performance errors of around 1 m.

It is interesting and informative to see where the relative navigation performance is poorest and best, especially as it relates to the number of visible GPS satellites. Figure 7 shows the combined three-axis error on the same plot with the GPS visibility, and as a general trend the filter performance improves with the number of visible satellites. Also of note in the filter performance is the ability to

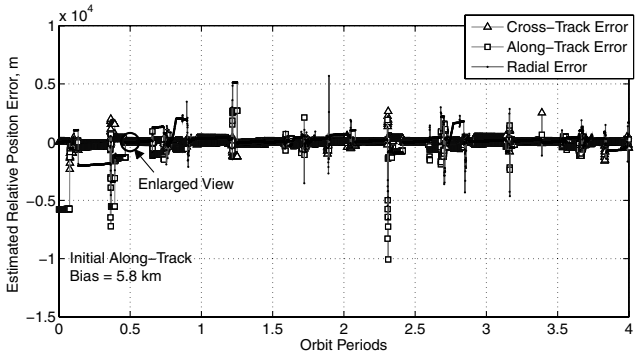

a) Relative navigation errors

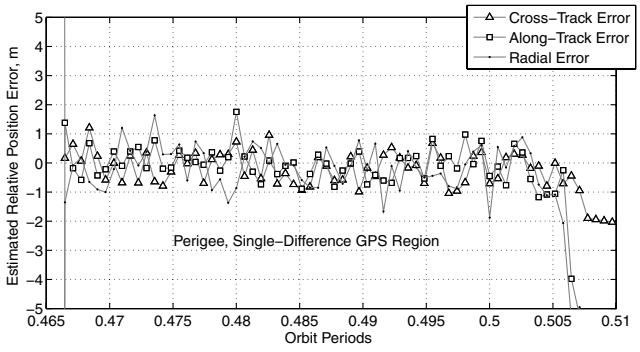

b) Enlarged view

Fig. 6 GPS only, relative position navigation error.

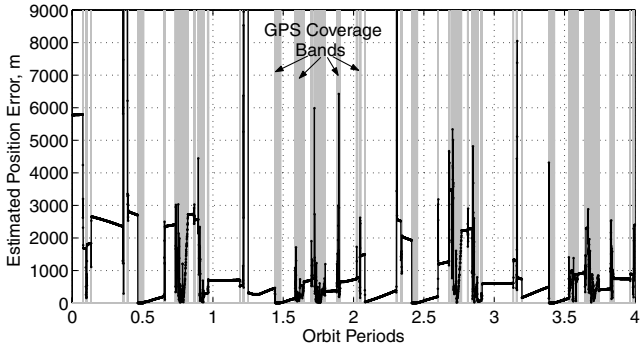

Fig. 7 GPS only, combined three-axis error shown with GPS availability.

correctly model and track the clock bias generated by the oscillator random walk. The typical oscillator parameters defined earlier were used. Figure 8 shows this error, and several large diversions are noticeable up to and exceeding 100 ms. Figure 9 shows the actual relative trajectory computed by the navigation filter. It is clear that many of the larger errors occur near apogee, as is expected when signal reception is often poorest.

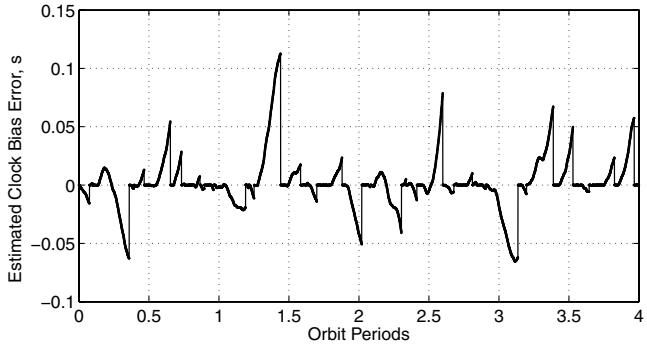

Fig. 8 GPS only, estimated clock bias error.

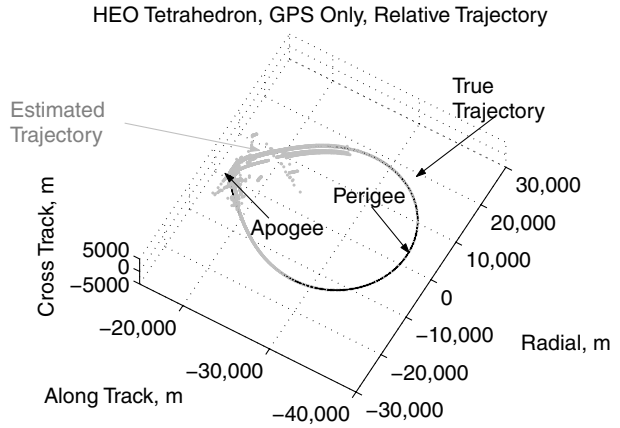

Fig. 9 GPS only, estimated relative trajectory for satellite 1.

Transponder-Only Navigation

Another sensor possibility is to use only onboard intersatellite transponders given some initialization by the GPS or DSN and then only tracking other members of the formation thereafter. Unlike the GPS-only case, the signals are always present and dead reckoning is not required. However, the small size and relative proximity of the formation can lead to geometric distribution problems. In addition, there is no external time reference for the formation and so any time-tagged data will be subject to timing errors pursuant to the estimated clock bias error of the filter. An alternative would be to allow one formation member to have a "master clock" that keeps formation time. This clock could be designed with low-drift characteristics and corrected periodically by ground command. Finally, the transponder does not provide absolute position knowledge, which is necessary to propagate the system equations of motion.

The relative position error estimates for the transponder-only case are shown in Fig. 10a. It is seen that the filter converges quickly from an initial bias. Large cross-track errors are obvious at particular locations in the estimate. These regions correspond to the locations where the formation becomes planar, losing all geometric distribution in the cross-track axis. There are radial and along-track errors on the order of a few meters, whereas cross-track errors can exceed 20 m in the worst-case geometries. A closer examination of this cross-track error is shown in Fig. 10b, in which the cross-track dilution of precision (DOP) confirms the location where the formation becomes planar and geometric distribution along that axis is lost. Clock estimator performance is shown in Fig. 11. Errors are seen to be in the 100–200 μs range, but grow larger as time elapses. This is expected because there is no absolute time reference and thus no way to observe and correct clock drift. It is also notable that, unlike the GPS-only case, position estimate errors at apogee are comparable to those at perigee.

Transponder and GPS Navigation

To overcome the shortcomings of the previous methods, a combined sensor suite may be used with a transponder system providing precise ranging while the GPS supplements with precise timing and differential corrections as visibility allows. This also provides an external time reference to facilitate the precise tagging of data collected by the formation and curtail long-term drift of the clock from absolute time.

The estimated relative position errors for the combined transponder and GPS case are shown in Fig. 12a. As in the transponder-only case, convergence occurs quickly. A closer view in Fig. 12b shows that the combined sensor filter is also subject to cross-track errors at the points where the formation becomes planar. This would suggest that singular geometries should be avoided when designing formations. There are insufficient GPS measurements in these areas to remove the associated errors. Figure 12b clearly shows the region in which the measurement-rich low-Earth-orbit (LEO) environment allows the relative GPS portion of the filter to drive

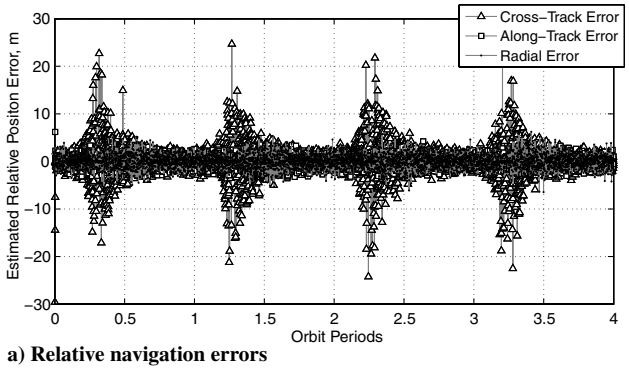

a) Relative navigation errors

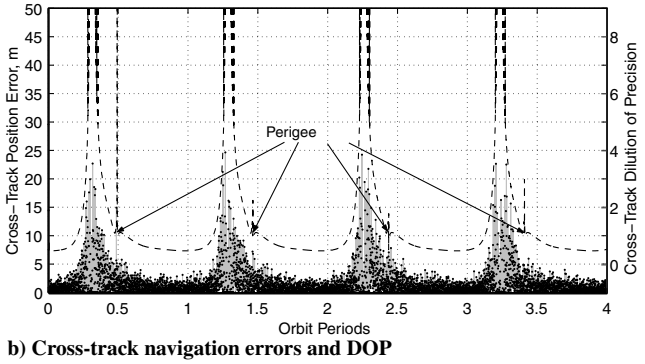

b) Cross-track navigation errors and DOP

Fig. 10 Transponder only, relative position navigation errors.

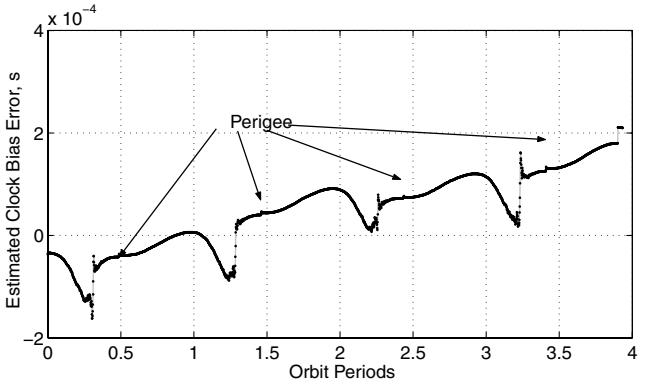

Fig. 11 Transponder only, estimated clock bias error.

errors to less than 1 m. This performance is typical for GPS carrier phase positioning and is superior to the transponder-only system in this region. As in the transponder-only case, an examination of the cross-track error displays the inherent weakness of the filter when the formation geometry is poor. A striking difference from all previous cases is seen, however, when the clock bias error estimate is examined in Fig. 13a. The transponder portion of the filter keeps outliers to a minimum, whereas the GPS portion updates and aligns the filter with the external time source. A closer view in Fig. 13b shows these realignments occurring. During the measurement-rich region close to perigee, timing accuracies better than 50 ns are seen.

The results of the simulation studies are shown in Tables 3 and 4. It is notable that the combined sensor type shows the best performance in most of the cases considered.

Libration Orbit Formations

In the restricted problem of three bodies, there are five points in the plane of motion where the gravitational forces of the two attracting bodies are balanced, described in detail by Szebehely and Mark [18]. Three of these libration points are collinear with the attracting bodies, whereas two are located at the vertex of an equilateral triangle formed by the attracting bodies.

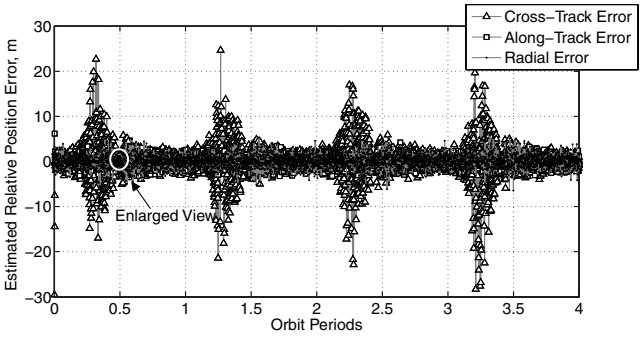

a) Relative navigation erors

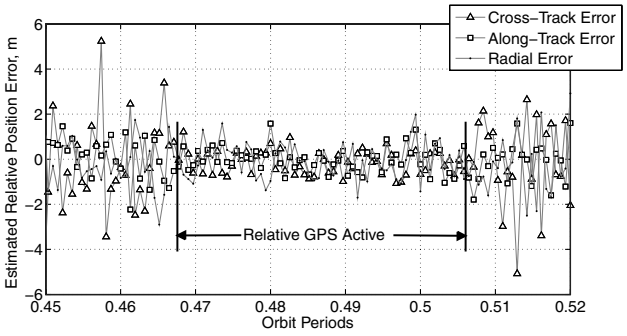

b) Enlarged view

Fig. 12 Combined transponder and GPS, relative position navigation errors.

A spacecraft can travel a semirepeating trajectory about a libration point known as a Lissajous orbit (Fig. 14a). When a collection of these satellites all travel slightly offset Lissajous orbits about the libration point, they can be arranged into a periodic formation. A satellite formation in an orbit about a sun–Earth libration point is of interest to many mission designers. For example, formations in these orbits may be used as large baseline interferometers for deep-space observation. Their distance from the Earth, around 1.5 million km,

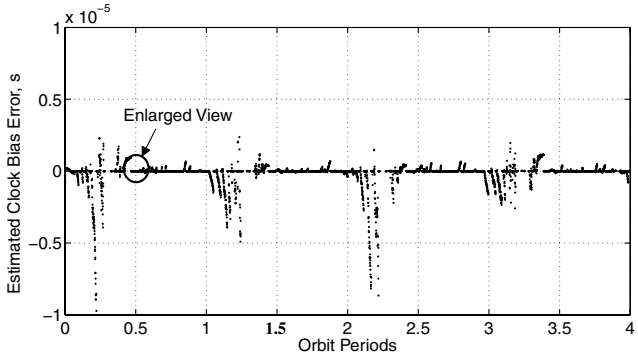

a) Estimated clock bias error

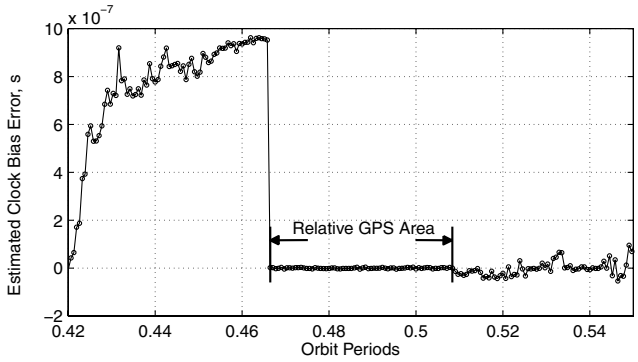

b) Enlarged view

Fig. 13 Combined transponder and GPS, estimated clock bias error.

Table 3 Root-mean-square error over four orbit periods

Sensor type	Radial, m	Along track, m	Cross track, m
GPS only	972.87	1032.4	268.44
Transponder only	1.4050	0.9679	2.8685
Combined	1.3748	0.9502	2.9376

Table 4 Root-mean-square error at perigee

Sensor type	Radial, m	Along track, m	Cross track, m
GPS only	1.2083	1.0016	0.5601
Transponder only	1.6720	1.0107	3.0691
Combined	0.7818	0.5860	0.5378

gives an observation environment with minimal radio interference. A mission of this type is baselined in Carpenter et al. [8] for use as a reference.

There are additional challenges with the formation navigation about a libration point. The relative equations of motion are very different from those of an LEO or HEO orbit. The orbit location is also outside the coverage of the GPS, and so relative navigation must be accomplished almost exclusively with onboard sensors. The formation geometry is also much slower changing that of the LEO or HEO.

Libration Simulation

The formation that was simulated for this study was based upon the libration benchmark orbit suggested by Carpenter et al.[8]. This study, like the HEO simulation, was performed as an example of many typical applications. Again, the sensor models developed in the previous sections were implemented in a dynamic simulation of Lissajous orbits. The reference orbit is shown in Fig. 14a. It involves a 300,000 km Lissajous orbit about the transterrestrial libration point, labeled L2 in Fig. 14a. The formation itself makes up an aspherical surface about the reference orbit with a radius of 250 m. The time-varying relative trajectories that this configuration produces are shown in Fig. 14b.

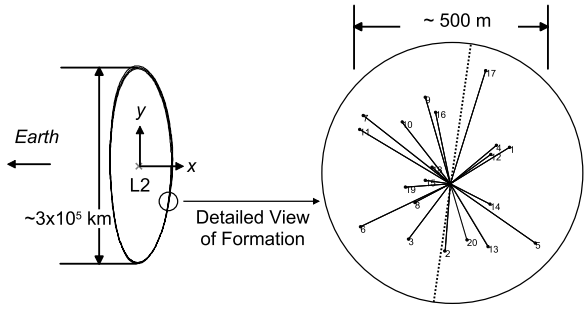

a) Aspherical formation

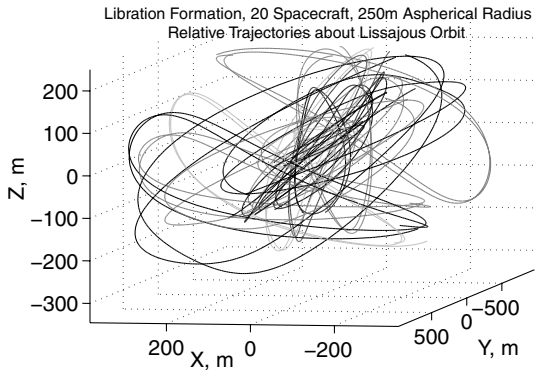

b) Relative trajectories

Fig. 14 Formation configuration about L2 Lissajous orbit.

Equations of Motion

The libration point orbit is an artifact of the restricted problem of three bodies. It is often derived in terms of a rotating reference frame containing the primary bodies and normalized to the distance between them. Neglecting disturbances, it is described by the following equations of motion [11]:

$$\ddot{x} = x + 2\dot{y} - \frac{1-\mu}{r_1^3}(x+\mu) - \frac{\mu}{r_2^3}(x-1+\mu)$$
$$\ddot{y} = y - 2\dot{x} - \frac{1-\mu}{r_1^3}y - \frac{\mu}{r_2^3}y \qquad \ddot{z} = -\frac{1-\mu}{r_1^3}z - \frac{\mu}{r_2^3}z \tag{39}$$

where

$$r_1 = \sqrt{(x+\mu)^2 + y^2 + z^3} \tag{40}$$

$$r_2 = \sqrt{(x-1+\mu)^2 + y^2 + z^3} \tag{41}$$

These equations of motion give the Lissajous orbit shown in Fig. 14a, whereas small variations in the initial conditions give rise to the relative trajectories shown in Fig. 14b.

Estimation Technique

The estimation technique employed for the libration simulation was very similar to that used in the transponder-only HEO case. The number of measurements, though, was much higher (19 vs 3), and so the size of the information and measurement matrices was adjusted accordingly. In addition, the equations of motion used for the prediction routine of the extended Kalman filter (EKF) were changed to match the Lissajous orbit dynamics.

Libration Results

As in the HEO case, it was assumed for this study that the phase measurements are taken with the integers properly resolved. All results presented are from the perspective of a single spacecraft (number 1 in Fig. 14a), as if the navigation filters are executing onboard that particular spacecraft. As in the HEO case, it is assumed that each member of the formation will be performing this task and exchanging estimated state information in the process. With 20 evenly distributed spacecraft in the formation, there are no geometric distribution problems as in the four-spacecraft HEO case. Because all of the relative navigation is self-contained in the formation, all timing information must be derived from oscillators aboard the spacecraft. The only exception is occasional contact with an Earth station such as NASA's DSN. This allows coarse initialization of the formation and time synchronization capabilities.

Figure 15a shows the relative position error of the EKF. The DSN ranging is able to provide some coarse initial formation knowledge, within about a kilometer along the Earth line-of-sight direction but only to within tens of kilometers out of plane [3]. Because of the coarse initial knowledge and the very slow geometry changes of this formation, the filter convergence takes longer than the LEO or HEO case. It is seen that the filter takes almost a full day to reach a converged navigation solution. Once converged, however, the relative positioning error remains less than 10 cm. The relative velocity error is shown in Fig. 15b. The convergence time is similar to that of the relative position, taking about a full day. Once converged, the errors remain less than 2 m/s. Figure 15c shows the clock drift errors in the EKF. The clock is derived from the random walk model described in the previous sections and, without an external reference, the errors grow without bound. The errors grow at a rate of about 6 ms/day and would affect the time tag of any data generated by this spacecraft. The estimated clock drift is shown in Fig. 15d. After convergence, errors were around 2–3 ns/s. Finally, the trajectory is shown in Fig. 16. It is seen that the solution estimate

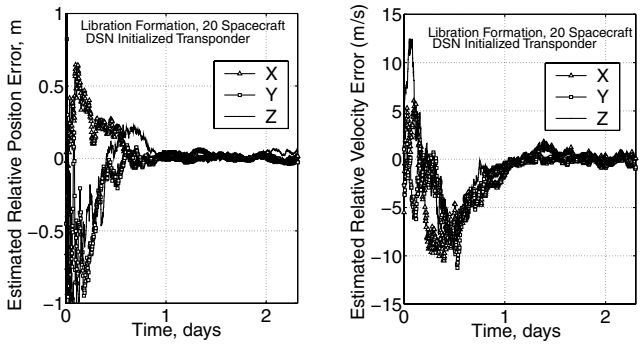

a) Estimated relative position error

b) Estimated relative velocity error

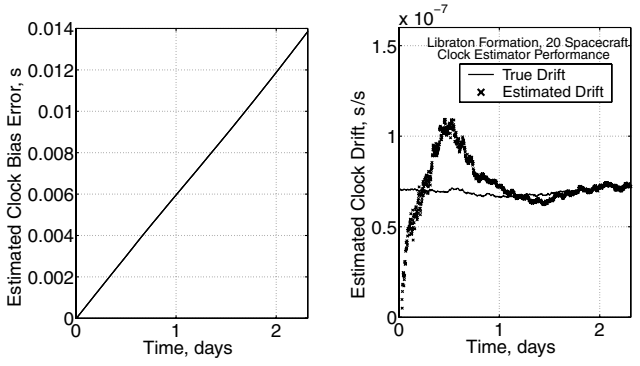

c) Estimated clock bias error (d_0)

d) Estimated clock drift (a_0)

Fig. 15 Libration formation estimated parameters.

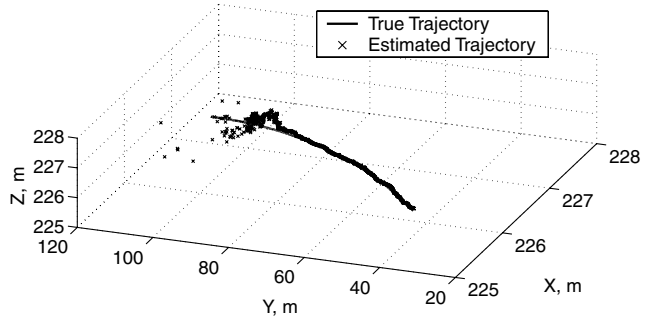

Fig. 16 Estimated trajectory of spacecraft 1.

converges from a coarse initial state onto the true trajectory and continues to track the relative navigation state. Because the transponder measurement is heavily dependent upon the well-estimated clock drift, the filter tracking performs well.

Conclusions

The objective of this paper was to investigate modelling, applying, and combining sensor measurements in a generalized spacecraft relative positioning algorithm for high-altitude and extraterrestrial missions. Mission designers can use these methods to incorporate multiple sensors, compare filter performance, and analyze noise sources.

There is much opportunity to build upon this research and further examine the topic of spacecraft formation flight. The analysis is notional in nature and is intended mainly to demonstrate the techniques that are used rather than to provide definitive measures of accuracy. Integer ambiguity techniques and multipath modelling were deliberately excluded from this study due to their mission-specific nature, but could be implemented if exploring a particular formation application. The estimated state could also be examined for elements to add or remove. For example, the clock bias term could be removed from a transponder-only filter and the spacecraft clock propagated from the clock drift estimate. Additional interformation sensors such as optical ranging devices could be modeled and incorporated into the filter routines. In addition, ground tracking could be included as an additional sensor measurement using the same combinatorial techniques. Relative formation attitude determination was also not considered in this study but is important to many formation flying missions.

Sensor and dynamic models could be further refined for specific missions or additional perturbation environments. In addition, formation design work could be performed with sensor considerations in mind. By avoiding unfavorable formation geometries that lead to high DOP, the relative navigation filter errors can be improved.

Acknowledgment

This research was carried out under NASA Cooperative Agreement NCC-5-732, monitored by M. C. Moreau, Flight Dynamics Analysis Branch, Goddard Space Flight Center.

References

[1] Kaplan, E. (ed.), *Understanding GPS Principles and Applications*, Artech House, Boston, 1996.

[2] Misra, P., and Enge, P., *Global Positioning System: Signals, Measurements, and Performance*, 2nd ed., Ganga–Jamuna Press, Lincoln, MA, 2006.

[3] Beckman, M., "Orbit Determination Issues for Libration Point Orbits," *Proceedings of the International Conference on Libration Point Orbits and Applications*, IEEC, June 2002, pp. 1–19.

[4] Moyer, T. D., *Formulation for Observed and Computed Values of Deep Space Network Data Types for Navigation*, Wiley–Interscience, New York, 2003.

[5] Ely, T. A., "Mars Network Radiometric Measurement Models and Data Interfaces for the Electra and CE-505 Radios," NASA Jet Propulsion Laboratory, Rept. IOM Electra-343K, Pasadena, CA, Oct. 2006.

[6] Parkinson, B. W., and Spilker, J. J., *Global Positioning System: Theory and Applications*, Vol. 1, AIAA, Reston, VA, 1996.

[7] Kovach, K., "New User Equivalent Range Error (UERE) Budget for the Modernized Global Positioning System (GPS)," *Proceedings of the ION National Technical Meeting*, Institute of Navigation, Anaheim, CA, Jan. 2000, pp. 550–573.

[8] Carpenter, J. R., Leitner, J., Folta, D., and Burns, R., "Benchmark Problems for Spacecraft Formation Flying Missions," AIAA Paper 2003-5364, Aug. 2003.

[9] Kelbel, D., Lee, T., Long, A., Carpenter, J. R., and Gramling, C., "Relative Navigation Algorithms for Phase 1 of the MMS Formation," *Flight Mechanics Symposium*, NASA, Greenbelt, MD, Sept. 2003, pp. 1–15;also NASA Paper CP-2003-212246.

[10] Gramling, C., Carpenter, J. R., Lee, T., and Long, A., "Relative Navigation Strategies for the Magnetospheric Multiscale Mission," *Proceedings of the 18th International Symposium on Space Flight Dynamics*, ESA, Munich, Oct. 2004, pp. 435–440.

[11] Vallado, David, A., *Fundamentals of Astrodynamics and Applications*, 2nd ed., Microcosm Press, El Segundo, CA, 2001.

[12] Wertz, James, R. (ed.), *Spacecraft Attitude Determination and Control*, D. Riedel Publishing Company, Boston, 1986.

[13] Tapley, B. D., Schutz, B. E., and Born, G. H., *Statistical Orbit Determination*, Elsevier, New York/Amsterdam, 2004.

[14] Broucke, R., "A Solution of the Elliptic Rendezvous Problem with the Time as Independent Variable," *Journal of Guidance, Control, and Dynamics*, Vol. 26, No. 4, July 2003, pp. 615–621.

[15] Littlefield, Ken, "Acquisition of GPS Signals for High Altitude Spacecraft Navigation: Exploring Issues in Visibility and Link Analysis," University of Colorado at Colorado Springs, Rept. A512943, Colorado Springs, CO, Jan. 1998.

[16] Moreau, M., Axelrad, P., Garrison, J., and Long, A., "GPS Receiver Architecture and Expected Performance for Autonomous Navigation in High Earth Orbits," *Navigation: Journal of the Institute of Navigation*, Vol. 47, No. 3, Fall 2000, pp. 191–204.

[17] Hofmann-Wellenhoff, B., Lichtenegger, H., and Collins, J., *Global Positioning System Theory and Practice*, Springer–Verlag, New York, 1997.

[18] Szebehely, V., and Mark, H., *Adventures in Celestial Mechanics*, 2nd ed., Wiley, New York, 1998.

D. Spencer
Associate Editor